

**INVESTIGATIONS OF QCD  
HADRONIZATION USING JETS  
MEASURED AT  $\sqrt{s} = 8$  TeV WITH  
THE ALICE DETECTOR.**

A Dissertation Presented for the

Doctor of Philosophy

Degree

The University of Tennessee, Knoxville

Andrew John Castro

March 2019

© by Andrew John Castro, 2019

All Rights Reserved.

# Chapter 1

## Quantum Chromodynamics

In 1968 deep inelastic scatterings performed at the Stanford Linear Accelerator Center showed that the proton had internal structure[1] called partons at the time. Within a decade of this discovery the partons were broken into two categories: the mass carrying fermions were known as the quarks and the gauge boson force carriers were called gluons. The interactions of these two types of particles were described by the quantum field theory known as Quantum Chromodynamics (QCD) and by the SU(3) symmetry group. SU(3) guarantees that color charge is conserved and this results in quarks grouping together into ‘colorless’ hadrons.

### 1.1 The QCD Lagrangian

QCD is the strongest of the known fundamental forces. It is a gauge field theory described by the Lagrangian density

$$\mathcal{L} = -\frac{1}{4}F_{\mu\nu}^\alpha F_\alpha^{\mu\nu} - \alpha_s(\bar{q}_j \gamma^\mu T_\alpha q_j)G_\alpha^\mu + \bar{q}_j(i\gamma^\mu \partial_\mu - m)q_j \quad (1.1)$$

where  $q$  and  $\bar{q}$  represent the color anti-color fields summed over color  $j$ ,  $\alpha_s$  is the strong coupling strength,  $\gamma^\mu$  is the Dirac gamma matrix,  $G_\alpha^\mu$  is the gauge field for color  $\alpha$ , is similar in analogy to the  $\mathbf{W}$  matrix from the electroweak theory.  $F_{\mu\nu}^\alpha$  is the field strength tensor and it describes the gluon interactions. The first term of the Lagrangian is the gluon contribution

and carries no mass term. The second term of the Lagrangian describes how quarks and gluons interact with each other. The final term describes quark interactions and the coupling between them and will be explored further in this thesis.

At short distances, less than  $0.2\text{ fm}$ , the strong coupling constant becomes exceedingly small and second term of the Lagrangian displays an important property known as asymptotic freedom[2].

$$\alpha_s = \frac{1}{\beta_0 \ln(Q^2/\Lambda^2)} \quad (1.2)$$

where  $\alpha_s$  is the strong coupling constant,  $Q^2$  is the momentum transfer between two interacting partons, and  $\Lambda^2$  is a cutoff below which QCD phenomena are strongly suppressed and  $\beta_0$  is a correction factor.

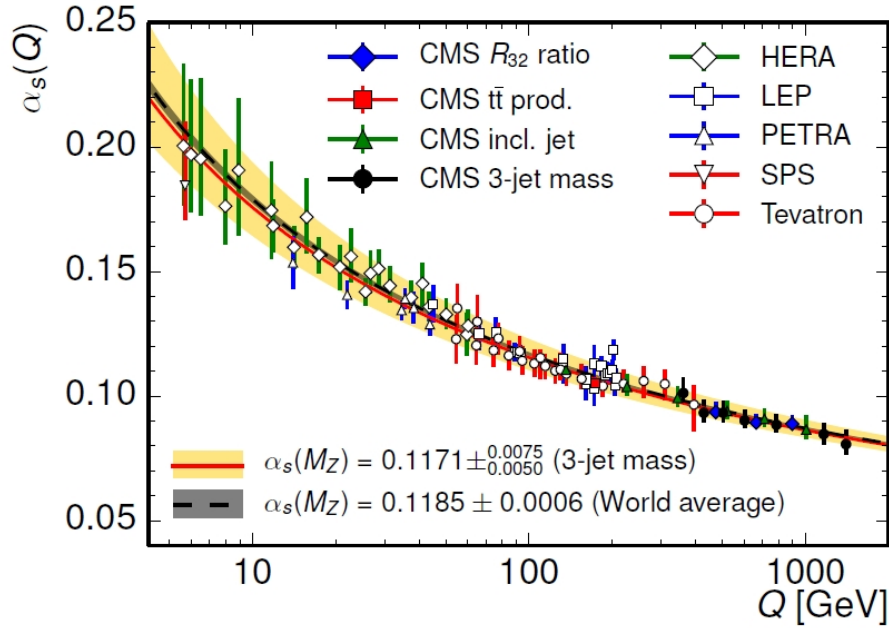


**Figure 1.1:** Strong coupling constant ( $\alpha_s$ ) as a function of the momentum transfer ( $Q$ )[3].

## 1.2 Jets

Hard probes (large  $Q^2$  interactions), are produced in the earliest stages of a high energy collision when the largest momentum transfer processes occur. As two highly energetic

partons propagate away from one another, in a back-to-back fashion, they will instigate a shower of daughter partons via gluon radiation and the generation of low-mass  $q\bar{q}$  pairs. These daughter partons will go on to form hadrons and the clustering of these hadrons is colloquially known as a ‘jet’. If the jet was created in a high energy experiment the final state hadrons will be recorded as tracks in a tracking detector or energy deposits in a calorimeter. This process is shown in Figure 1.2.

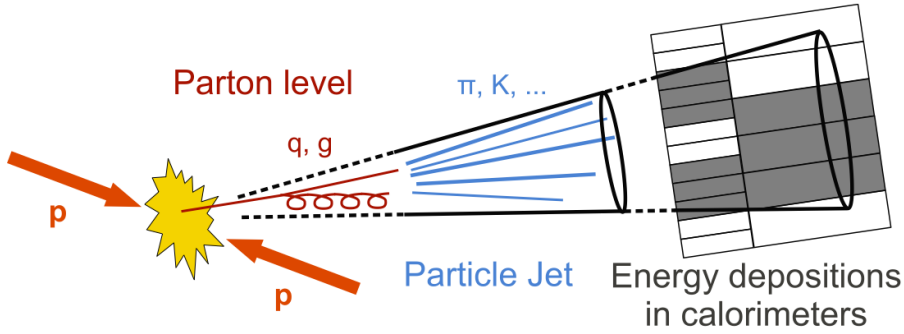


**Figure 1.2:** Diagram showing a jet created by two partons under going a hard scattering, forming into hadrons, and detected in a calorimeter[4].

The physicist James Daniel Bjorken postulated that a correlation could be surmised by summing over the final state transverse momentum of the hadrons that form a jet to the parton that initiated the hard scattering[5][6]. This has lead to jets becoming the work-horse for both experimentalists and theorists over the past 30 years in probing QCD phenomena. This thesis makes use of jets as an important probe of QCD and the following sections are devoted to developing a background for both the theoretical and experimental treatment of jet physics. The following sections will be devoted to how jets are produced from a physics point-of-view and the latest results which this thesis compares to.

### 1.2.1 Jet Production and the Factorization Theorem

Due to confinement bare quarks are unobserved, therefore experimentalists must probe QCD interactions by detecting the color neutral final state hadrons measured in collider experiments. Fortunately, the factorization theorem (Equation 1.3) allows for the final state jet cross section to be broken into a number of steps that can either be calculated

perturbatively using pQCD or modeled phenomenologically. Using the factorization theorem the jet cross section in a pp collision is,

$$d\sigma^{pp \rightarrow jet} \sim f_{a/A}(x_1, Q^2) \otimes f_{b/B}(x_2, Q^2) \otimes d\sigma_{ab \rightarrow c+X}(x_1, x_2) \otimes D_{c \rightarrow h/jet}(z, Q^2) \quad (1.3)$$

- $f_{a/A}(x_1, Q^2)$  and  $f_{b/B}(x_2, Q^2)$  are the parton distribution functions (PDF) that describe the probability of finding parton,  $a$  or  $b$ , within nuclei,  $A$  and  $B$ , with a given momentum fraction,  $x = p_{parton}/p_{hadron}$  as a function of  $Q^2$ .
- $d\sigma_{ab \rightarrow c+X}(x_1, x_2)$  is the pQCD parton-parton cross section due to the hard scattering of the two partons,  $a$  and  $b$ , to an intermediate parton ( $c$ ).
- $D_{c \rightarrow h/jet}(z, Q^2)$  is the fragmentation function (FF) that describes the probability the an outgoing parton,  $c$ , fragments and hadronizes into a final state hadron,  $h$ , within a jet with momentum fraction,  $z \equiv p_{hadron}/p_{parton}$ .

Figure 1.3 shows a timeline of a pp collision broken into the relevant steps in accordance to the factorization theorem. One of the best places to fundamentally test QCD phenomena using hard probes, i.e. jets, are with high energy hadron colliders such as those found at CERN<sup>1</sup>, Fermilab, and BNL. The time scale that a hard probe is created in a high energy collision is on the order of  $\tau \approx 1/p_T \approx 0.1 \text{ fm}/c$  which probes the initial state these interactions. The factorization theorem allows for a high level of agreement between the QCD theory of nature and experimental observables but to ascertain this connection we should discuss each term of the factorization theorem in more depth.

## Parton Distribution Functions

The PDF occurs twice in Equation 1.3 due to the two partons that will undergo the hard scattering being confined in two different protons. PDFs may be thought of as conveying the structure of a nucleon in terms of the number of flavored quarks or gluons ( $u(x)$ ,  $d(x)$ ,

---

<sup>1</sup>Discussed in detail in Chapter 3

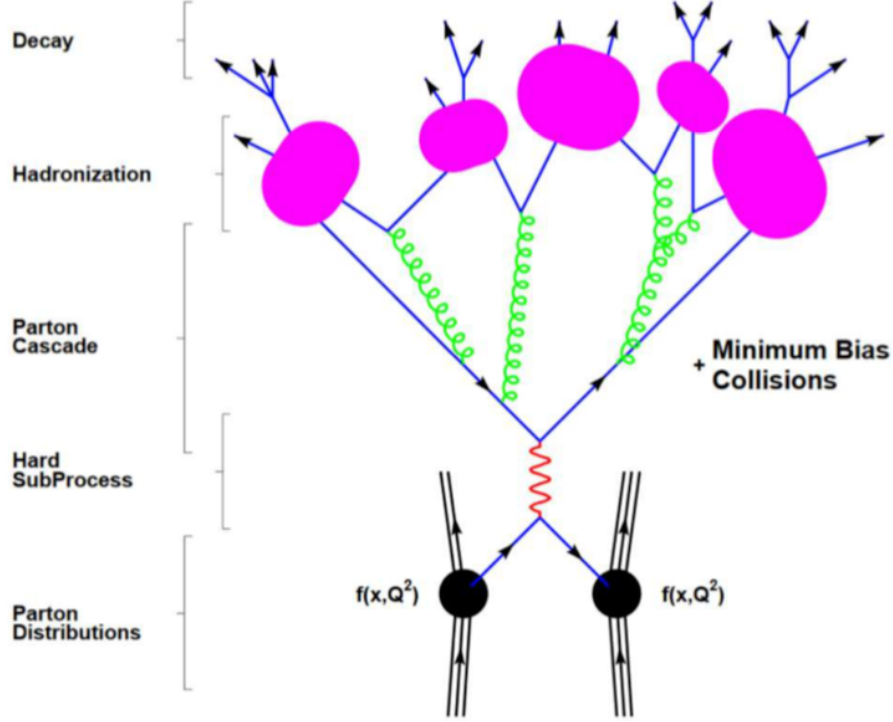


**Figure 1.3:** Timeline of a proton-proton collision. Starting from the bottom, two partons confined within the colliding protons have a hard interaction. The outgoing partons will induce partonic showers by radiating quarks and gluons. The partonic showers will eventually form into final state hadrons due to confinement which are measured in high energy experiments[7].

$s(x), \bar{u}(x), \bar{d}(x), \bar{s}(x), g(x)$ ) and must obey certain constraints and summation rules. In the case of a proton, with electric charge ( $e = +1$ ),

$$+1 = \frac{2}{3} \int_0^1 [u(x) - \bar{u}(x)] dx - \frac{1}{3} \int_0^1 [d(x) - \bar{d}(x)] dx \quad (1.4)$$

and isospin ( $I = 1/2$ ),

$$\frac{1}{2} = \frac{1}{2} \int_0^1 [u(x) - \bar{u}(x)] dx - \frac{1}{2} \int_0^1 [d(x) - \bar{d}(x)] dx \quad (1.5)$$

have a solution,

$$\int_0^1 [u(x) - \bar{u}(x)] = 2 \quad (1.6)$$

$$\int_0^1 [d(x) - \bar{d}(x)] dx = 1 \quad (1.7)$$

This corresponds to the classical partonic view that protons contained two up quarks and a down quark, similarly the neutron, with charge  $e = 0$  and isospin  $I = -1/2$ , can be shown that it compromises two down quarks and a up quark. Naively, we could assume that the three quarks composing a proton would each carry a momentum fraction of approximately  $1/3$  the total momentum of a proton. However, high energy deep inelastic scattering experiments conducted at the Stanford Linear Collider in the 1960's[8] measured the momentum carried by the three quarks only accounting for about  $1/2$  the total proton momentum. This lead to a more complex and dynamic model of the proton structure with the other half of the proton momentum being occupied by neutral partons which would eventually become known as gluons.

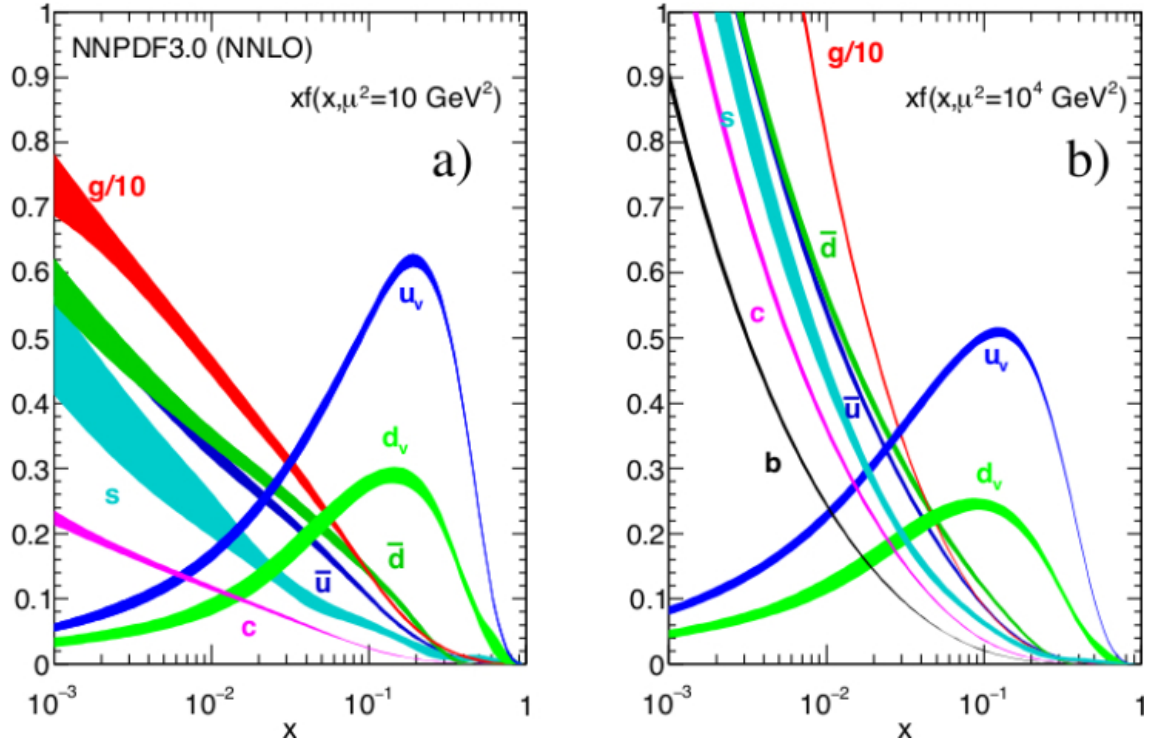


**Figure 1.4:** Proton PDF at  $Q^2 = 10 \text{ GeV}$  (left) and  $Q^2 = 10 \text{ TeV}$  (right) from the NNPDF Collaboration[9].

Measuring the structure of the partons making up a nucleon is a major endeavor by both theorists and experimentalists. Two of the most popular PDFs available to physicists are the CTEQ[10] (Coordinated Theoretical-Experimental Project on QCD) and the NNPDF[11] (Neural Network Parton Distribution Function) sets. Figure 1.4 shows the proton PDF as

a function of the momentum fraction for two energy ranges, at high values of  $x$  the two up quarks account for about 2/3 of the momentum fraction while down quark accounts for about 1/3 the total momentum, these quarks are collectively called the valence quarks. At high energies, low values of  $x$ , we see that the proton has non negligible contributions from gluons, anti-quarks, strange, and even charm quarks, these are collectively known as the sea partons. Today, the modern picture of a protons structure is that it is mostly composed of gluons and sea quarks at low values of  $x$  and this domination only increases as a function of  $Q^2$ [12].

### Parton-Parton Cross-Section

The parton-parton cross section can be calculated using perturbation theory. To the zeroth order in  $\alpha_s$  this cross-section would be a simple quark-antiquark annihilation and would be calculable using Feynman diagrams as seen in Figure 1.5[13]. Higher ordered contributions, such as the creation of virtual gluons, require the hard cross-section to be expanded as a series in terms of  $\alpha_s$ . Calculations of the hard cross section that incorporate these higher order terms are known as *next-to-leading order* (NLO) with  $N$  denoting the number of terms after the leading order that have been included in the cross-section calculation. Various calculations of the hard cross-section of different QCD processes have been performed over the years typically using either power series or logarithmic expansions of  $\alpha_s$ [14] and corrections for LO, NLO, and even NNLO constitutes a very active field in high energy physics.

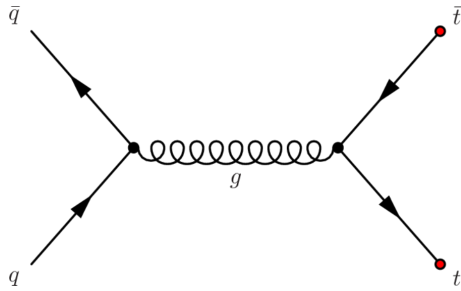


**Figure 1.5:** Lowest order quark-antiquark annihilation to top-antitop pair[15].

Perturbative techniques of the hard cross-section have been extremely successfully in describing jet features in hadronic collisions[12].

## Hadronization

Hadronization is the process by which the colored pQCD partons of form into colorless non-pQCD hadrons and represents a significant barrier in progressing jet physics. This is due to the fact that hadronization encompass several smaller processes which in themselves are hard to characterize. Thus, like PDFs, an accurate description of hadronization requires a phenomenological approach by which experimental results help complement theoretical calculations. Jet production via hadronization[16] follows two distinct stages. First, the partons that underwent a hard scattering start to emit radiation via gluon bremsstrahlung up until time,  $t < Q^2$ , this is known as the parton cascade. The parton cascade is the precursor of what will become a jet as most of the radiation generated will travel in the same direction as the initial hard scattered parton. However, this immediately poses an issue in jet physics as radiation generated at a wide angle away from the momentum axis of the initial hard scattered parton will not be associated with the jet.

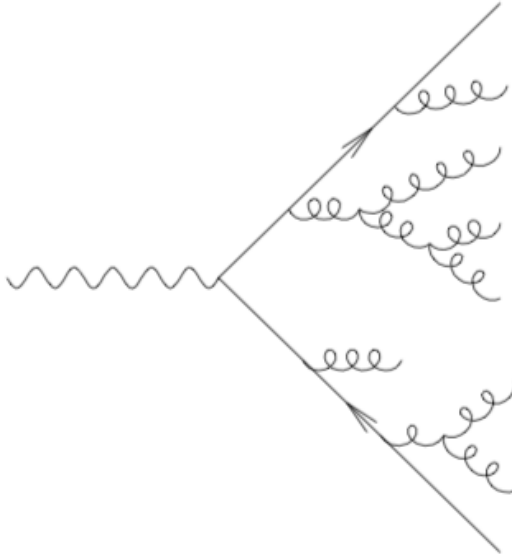


**Figure 1.6:** Parton cascade in a hadronic collision[16].

After the cascade has ended the partons must fragment into color neutral hadrons. There are two main phenomenological models used to describe the hadron forming process, the Lund String Model and the Cluster Hadronization Model. The QCD potential is,

$$V(r) = -\frac{\alpha_s}{r} + \sigma r \quad (1.8)$$

where the first term of Equation 1.8 goes as the Coulomb potential with a  $1/r$  dependence and is the dominate term at short distance and the second term has a string-like potential with  $\sigma$  referring to a string-like tension. The Lund String Model ignores gluon radiation and has fragmentation occur via breaking the string tension with the production of  $q\bar{q}$  sea quarks. The created sea quarks will carry some momentum fraction,  $z$ , of the initial parton until  $z$  falls below some cutoff. Figure 1.7 shows a two quarks undergoing a string breaking, each of the quarks initiating the string breaking will combine with a sea quark in an iterative manner to form hadrons.

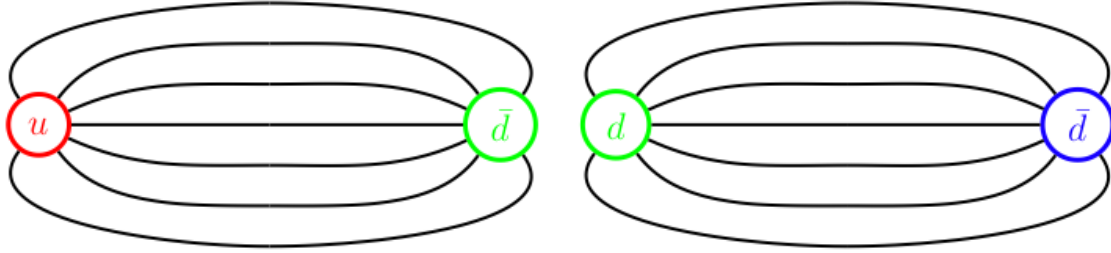


**Figure 1.7:**  $u\bar{d}$  generating a  $d\bar{d}$  pair via string breaking which will form color neutral hadrons, black lines show the string like equipotentials.[17].

The Cluster Hadronization Model has gluons splitting after the parton cascade phase into  $q\bar{q}$  pairs. These pairs will form color-singlet clusters with other neighboring quarks in phase-space. These color-singlets will typically be a few  $\text{GeV}/c^2$  in mass and are treated as excited meson resonances. These psuedo-resonances will decay via their normal branching ratios into the stable hadrons[18].

## Fragmentation

Similar to how a PDF quantitatively describes the structure of a nucleon the FF quantitatively describes the hadronization process. The FF is also similar to the PDF in that it is also a probability distribution, thus it follows the probabilistic rule that,

$$\sum \int z D_{c \rightarrow h/jet}(z, Q^2) dz = 1 \quad (1.9)$$

Ideally, the fractional momentum of the hadrons created from the fragmenting parton,  $z \equiv p_{\text{hadron}}/p_{\text{parton}}$ . Due to the confinement of partons we must use a suitable substitution for measuring the FF. The Parton-Hadron Duality[19] states that a hadron found near the center of a jet should encompass the quantum numbers and kinematic properties associated with the hard scattered quark that initiated the jet. Thus we can measure the fragmentation function as  $z = p_{\text{hadron}}/p_{\text{jet}}$ . The formulation of the FF as a fractional energy carried by the hadrons in a jet was a breakthrough in pQCD techniques and is analogous to how an electron passing through an absorber creates photon showers with these photons generating conversion electrons until the total energy has been dissipated into the material.

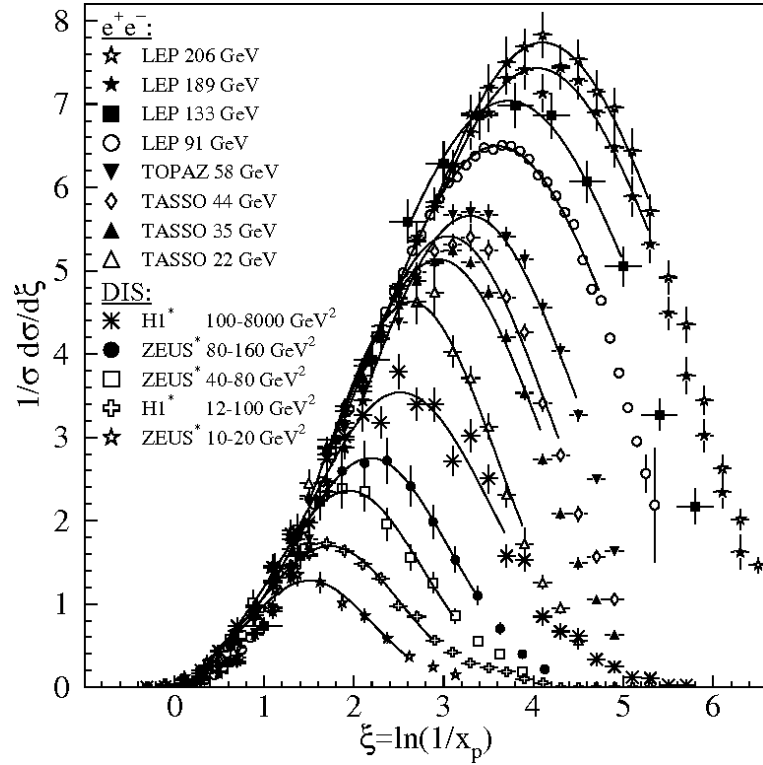


**Figure 1.8:** Fragmentation Functions from  $e^+e^-$  and DIS experiments with fits[20].

Figure 1.8 is the FF in terms of the Gaussian equation,  $z dN/dz = -dN/d\xi$  with  $\xi = -\ln 1/z$ . The observation that the Gaussian peaks of Figure 1.8 along with the suppression of the FF at low  $z$  values due to gluon coherence were predicted by pQCD.

## 1.3 Jet Finding Algorithms

A jet arises from the fragmentation of a hard parton to final state hadrons. However, grouping the hadrons together into a jet is a non-trivial task and jet finding algorithms are deployed in order to achieve this objective. Early on in jet physics, both theorists and experimentalists used a wide variety of jet finders that made comparisons between experiments or to theoretical calculations nearly impossible[21]. For example, a radiated gluon that splits into a quark anti-quark pair may become one or two jets depending on the angular separation and the algorithm used. Early jet finders tended to be sensitive to soft particles or could give widely varying yields to the number of jets in an event. In 1990, the Snowmass Accord[22] was held in order to standardize the definition of a jet between experimentalists and theorists. The agreement maintained that any algorithm that clusters particles into a jet must be both infrared and collinear safe (IRC).

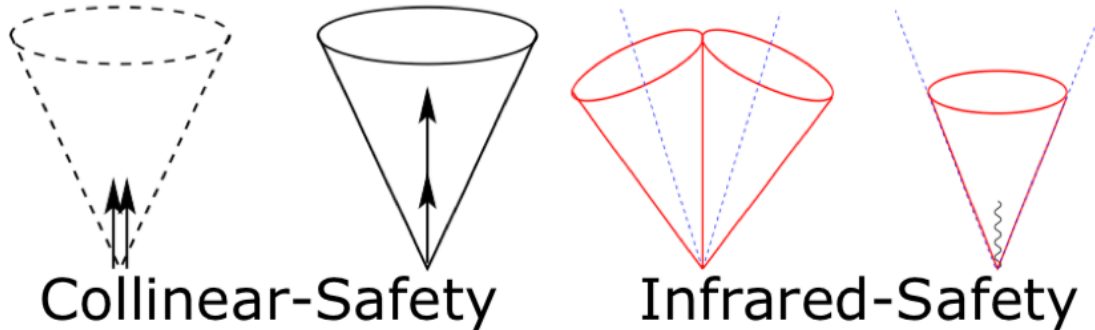


**Figure 1.9:** Cartoon showing Collinear and Infrared safe jet candidates[23].

Collinear safety ensures that a high- $p_T$  particle split into two or more particles should not influence the kinematics of a hard jet, this makes the jet finders insensitive to how hadrons are grouped together. Infrared safety in turn requires that the emission of soft radiation should not affect the properties of a jet, this makes jets returned by the algorithm independent of soft physics and a true signature of a hard process. Both of these processes are shown in Figure 1.9. After the adoption of these standards from the Snowmass Accord, old algorithms that violated these rules were patched and new jet finders were developed to comply with IRC safety. The most prevalent jet finding algorithms today fall into two categories: cone algorithms and sequential recombination/clustering algorithms.

### 1.3.1 Cone Algorithms

Cone algorithms made up the bulk of early jet finders. The only IRC safe cone algorithm still in use today is the seedless infra-red safe cone algorithm (SIScone). SIScone defines a cone of radius, R, around the highest momentum particle in the coordinates of  $(\eta, \phi)$ <sup>2</sup>, this is the proto-jet. SIScone then proceeds through an iterative process of finding all the particles within the jet radius such that  $R \leq \sqrt{\phi^2 + \eta^2}$  and calculates a new jet center based on these particles momenta and a new weighted jet axis  $(\eta, \phi)$ . If the new center matches the proto-jet center, the proto-jet is tagged as a stable jet, all the particles in that jet are removed, and SIScone moves onto the next highest  $p_T$  particle. Cone algorithms tend to be unpopular due to being computationally expensive, they are hard to implement theoretically, and can give results not calculable in perturbation theory.

### 1.3.2 Sequential/Recombination Algorithms

The other class of jet finders are the sequential/recombination algorithms, which are favored by experimentalists, theoreticians and are IRC safe. There are three types of sequential/recombination algorithms:  $k_T$ , Anti- $k_T$ , and the Cambridge/Aachen jet finders, with  $k_T$  referring to the transverse momentum of particle. All of the algorithms use a similar method, first they find the distance between every pair of particles,  $d_{i,j}$ , such that

$$d_{i,j} = \min[p_{T,i}^a, p_{T,j}^a] \frac{\Delta_{ij}^2}{R^2} \quad (1.10)$$

where  $p_{T,i}^a$  is the transverse momentum of particle  $i$ ,  $a$  is free parameter that is set based on which algorithm is used,  $\Delta_{ij}^2 = (\eta_i - \eta_j)^2 + (\phi_i + \phi_j)^2$  is the distance between the particles, and  $R$  is the radius of the jet. A second distance is defined in the sequential/recombination algorithm scheme,

---

<sup>2</sup>It is possible to use a Cartesian coordinate system in particle colliders, with the z-component referring to points along the beam axis while the xy-plane is perpendicular to the beam axis. However, this system is not invariant under a Lorentz boost. Therefore it is more useful to use the cylindrical-like coordinates of pseudorapidity ( $\eta$ ) and the azimuthal angle ( $\phi$ ). Pseudorapidity may be thought of as the polar angle in a cylindrical coordinate system with  $\eta = 0$  when the polar angle is perpendicular to the beam axis and  $\eta = \infty$  along the beam axis.  $\phi$  is the azimuthal angle that rotates around the beam axis. Both,  $\eta$  and  $\phi$  are invariant for Lorentz boosts along the beamline and allow for easy comparisons between the center-of-mass frame and the laboratory frame of a high energy collision.

$$d_{i,B} = p_{T,i}^a \quad (1.11)$$

this is the distance between a given particle  $i$  and the beam axis. Sequential/Recombination algorithms find the set of all particles,  $d_{i,j}, d_{i,B}$ , such that if  $d_{i,B}$  is the minimum for particle  $i$  it is tagged as a jet and removed from the list. If  $d_{i,j}$  are a minimum for particles  $i$  and  $j$  these two particles are merged together into a new particle  $(ij)$  and a new minimum is found between  $(ij)$  and particle  $k$  until all the particles are either merged into jets or the minimization function is no longer satisfied.

### $k_T$ Algorithm

The  $k_T$  algorithm sets the value  $a$  to 2, this results in a minimization function,

$$d_{i,j} = \min[p_{T,i}^2, p_{T,j}^2] \frac{\Delta_{ij}^2}{R^2} \quad (1.12)$$

which clusters low momentum particles first, making this algorithm susceptible to the underlying event (UE) or pile-up (PU). Thus the  $k_T$  algorithm is good at estimating any background present in a high energy collision.

### Anti- $k_T$ Algorithm

The Anti- $k_T$  algorithm sets the value  $a$  to -2, resulting in a minimization function,

$$d_{i,j} = \min\left[\frac{1}{p_{T,i}^2}, \frac{1}{p_{T,j}^2}\right] \frac{\Delta_{ij}^2}{R^2}. \quad (1.13)$$

The minimization function is dominated by high- $p_T$  particles, thus the area and axis of a jet is only slightly perturbed by soft particles. This makes the Anti- $k_T$  algorithm robust in jet finding with events having a UE and PU. The Anti- $k_T$  algorithm is the default jet finding algorithm used at the Large Hadron Collider and is the one used in this thesis.

### Cambridge/Aachen Algorithm

The Cambridge/Aachen algorithm sets  $a$  to 0 and this results in a minimization function of,

$$d_{i,j} = \frac{\Delta_{ij}^2}{R^2} \quad (1.14)$$

which makes it independent of particle momentum and sensitive to PU and UE. Due to the fact that the Cambridge/Aachen algorithm is only dependent on the particle coordinate it is most useful in studying jet structure.

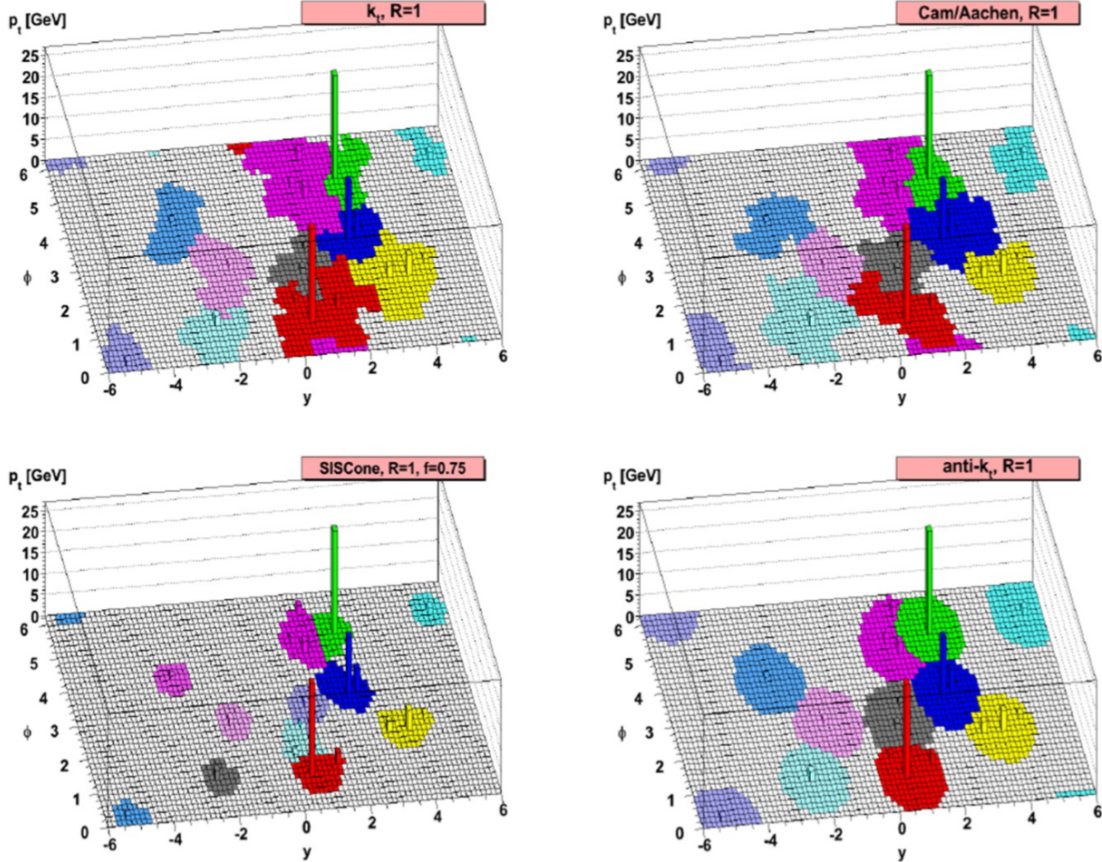


**Figure 1.10:** Lego plot of all four jet finders used on a single event with  $R = 1$  jet radius[21].

Figure 1.10 shows the jets found in a single event using all four jet finding algorithms. It should be noted that the Cambridge/Aachen and  $k_T$  algorithms have highly irregular and large shapes, making them both susceptible to the presence of a UE, while SIScone finds an additional jet due to splitting. The Anti- $k_T$  algorithm finds circular jets which demonstrates its robustness to hard radiation.

Once a stable jet is found, a recombination scheme is deployed in order to garner the jet kinematics. By adding the 4-vector,  $\mathbf{p}^\mu = (\mathbf{E}, \mathbf{p}_x, \mathbf{p}_y, \mathbf{p}_Z)$ , for all of the associated particles

composing a jet, we may obtain the jet momentum, energy, coordinates, etc<sup>3</sup>. In a particle collider with the tracks from a tracking detector measuring particle momentum and the towers of a calorimeter measuring particle energy we obtain the following relationships

$$p_T^{jet} = \sum_{particles} p_T = \sum_{tracks} p_T \quad (1.15)$$

$$E^{jet} = \sum_{particles} E = \sum_{towers} E \quad (1.16)$$

$$\eta^{jet} = \frac{1}{2} \ln \left( \frac{|\mathbf{p}^{jet}| + p_L^{jet}}{|\mathbf{p}^{jet}| - p_L^{jet}} \right) \quad (1.17)$$

$$\tan \phi^{jet} = \frac{p_y^{jet}}{p_x^{jet}} \quad (1.18)$$

where  $p_L$  refers to the longitudinal momentum which is the momentum component parallel to the beam axis. This method of adding the 4-vector of the particles composing the jet together in order to gain the jet kinematics is known as the E-scheme[24].

### 1.3.3 FastJet

FastJet[24] is a C++ software package that performs jet finding. Due to the computational efficiency, ease of use, and straight forward implementation, FastJet is the de-facto preferred jet finder used by theoreticians and all current high energy experiments. It implements the four previously discussed jet finders along with both the E-scheme and a boost invariant  $p_T$  scheme (BIpt-scheme) for recombination. The BIpt-scheme obtains the jet momentum and energy in the same manner as the E-scheme but uses a weighted average to find the jet coordinates,

$$\eta^{jet} = \sum_{particle} \frac{p_T^{particle}}{P_T^{jet}} \eta^{particle} \quad (1.19)$$

---

<sup>3</sup>For a review of relativistic kinematic see Appendix ...

$$\phi^{jet} = \sum_{particle} \frac{p_T^{particle}}{P_T^{jet}} \phi^{particle} \quad (1.20)$$

In addition to basic jet measurements, FastJet contains a number of advance features, which allows it to be used to study jet area, jet substructure, and jet background subtraction[25].

## 1.4 Monte-Carlo Generators

Monte-Carlos (MC) allow for the simulation of high energy events on a statistical basis. Particle level generators use different phenomenological models of the factorization theorem in order to simulate the energy, momentum, particle species, multiplicity, and direction of travel expected in a high energy collision. In order to validate an analysis the particle level simulations are further propagated through a detector level simulation of an experiment, such as Geant3[26], in order to negate detector effects on the output observables from the MC simulation. In this section only the particle level simulations used in the thesis are discussed.

### 1.4.1 PYTHIA

PYTHIA[27], is a C++ Monte Carlo software tool-kit used to model proton-proton collisions. The package uses pre-defined parton distribution functions as input afterwards it simulates the partonic showers and radiation due to a hard scattering by generating the LO scattering matrix elements. Hadronization is performed in PYTHIA using the Lund String Model. After which relative branching ratios are used to statistically throw the decay modes of the hadrons until they are stabilized.

PYTHIA underestimates jet production due to the limitations of using LO calculations. Therefore, it uses an arbitrary value (K-factor) to make NLO corrections to the LO cross section. The K-factor is defined as,

$$K = \frac{\sigma_{NLO}}{\sigma_{LO}}. \quad (1.21)$$

NLO corrections to the cross-section will not match experimental results, PYTHIA implements additional phenomenological adjustments used to better match data. PYTHIA encompass these corrections into sets known as ‘tunes’, with PYTHIA 6.4 Perugia-2010 tune being used for this analysis[28].

### 1.4.2 PHOJET

PHOJET is a FORTRAN 77 Monte Carlo simulator used to model proton-proton collisions. It is an alternative to PYTHIA and is better at modeling soft physics processes present in high energy collisions. PHOJET implements the Dual Parton model[29][30] and multiple parton interactions[31] to model soft physics. Hard interactions are implemented in PHOJET using LO scattering elements and it uses PYTHIA for the fragmentation and hadronization phase. Due to its ability to model soft physics, PHOJET is better at comparing to minimum bias<sup>4</sup> data and understanding jet results in a low kinematic range. PHOJET also acts as a benchmark in understanding any bias due to using other MC generators, such as PYTHIA. PHOJET v1.2 is used in this thesis.

## 1.5 The Quark-Gluon Plasma

At the temperatures and pressures typical to the Universe today nuclear matter is confined to a colorless hadronic gas. However, it was theorized that at extreme temperatures, such as those experienced in the early Universe, partons would have undergone a phase transition where by they were no longer bound to a color neutral state. This state of matter would have been analogous to a conventional plasma where by the electrons are no longer bound to a nucleus, thus the state was dubbed the Quark-Gluon Plasma (QGP). The nuclear phase diagram is shown in Figure 1.11 as a function of temperature and the net baryon density. Normal nuclear matter is confined to the bottom left while increasing temperatures and/or densities correspond to the QGP. Modern particle colliders , such as RHIC and the LHC, are able to obtain the densities and temperatures necessary to create a QGP and are likewise shown in the figure. The reason for particle colliders being located at low baryon density

---

<sup>4</sup>Events with a low total transverse momentum and high cross section

is due to the fact that at high  $Q^2$  energies more quark antiquark pairs are produced. This dilutes the total baryon density in the initial system and is more akin to what the early Universe was like.

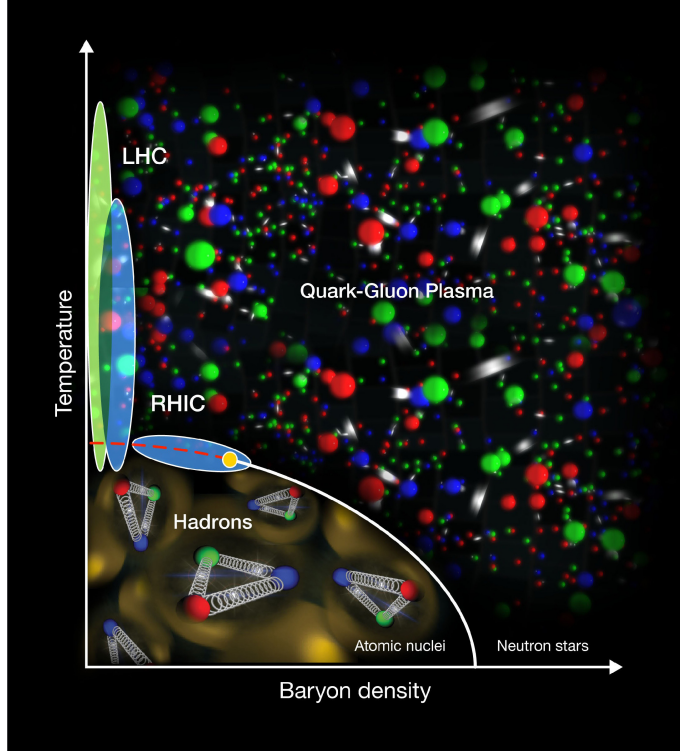


**Figure 1.11:** The QCD phase diagram[32].

### 1.5.1 Nuclear Collisions

By colliding heavy nuclei together in high energy collisions it is possible to obtain the energy densities and temperatures associated with the QGP state. The first signatures for the QGP were measured via a  $J/\psi$  suppression at the Super Proton Synchrotron located at CERN in 2000[33]. In 2005, the four experiments on the RHIC collider: BRAHMS[34], PHENIX[35], PHOBOS[36], and STAR[37], co-announced the observation of a new state of matter consistent with the hot and dense QGP. Surprisingly, the results from RHIC pointed at the QGP behaving more like a perfect fluid over a plasma-like state[38]. The QGP offers a rich and dynamic environment to test QCD predictions under some of the most extreme circumstances. Figure 1.12 shows the difference between a proton-proton collision

and a heavy-ion collision. The heavy-ion collision mirrors the processes in a proton-proton collision (left) described in depth in Section 1.2.1. After the initial hard scattering the phase transition to a QGP occurs. The QGP undergoes a hydrodynamical evolution and expansion until it cools to a colorless hadronic gas. After the phase transition occurs unstable hadrons will decay until they are stable at which point the final state particle composition is set and the chemical freeze out occurs. The hadron gas expands and cools until all soft interactions cease, this is the kinetic freeze out, after which the final momentum spectra is set.

### 1.5.2 Jets as a Probe of the QGP

Jets are an excellent probe of the thermodynamic properties of the QGP. This is due to them being produced in the earliest stages, before the formation of the QGP, and surviving the full evolution of a heavy-ion collision. As a jet propagates through the QGP it will lose energy to the medium through a combination of gluon radiation to the colored medium and inelastic scatterings. These energy loss mechanisms are dependent on the distance a parton travels through the QGP and on the species of the parton.

Figure 1.13 shows two back-to-back partons undergoing a hard scattering. Both will fragment into jets, but the first parton with transverse energy,  $E_{T1}$ , will be subjected to much less energy loss over the second parton due to the first parton only traveling through the outer edge of the QGP. The species dependent parton energy loss arises from kinematic constraints to gluon emission from the heaviest of quarks. This radiation is suppressed at angles smaller than the ratio of the quark mass to its energy and has been dubbed the *Dead-Cone Effect*. Tagging the flavor dependence of jets, either via measuring electrons from semi-leptonic decays or reconstructing the secondary vertex of heavy flavor mesons, has recently shown that energy loss via the Dead-Cone effect is strongly suppressed with jets containing a charm quark[40].

One way of quantifying the energy loss in a heavy-ion collision is via measurements of the nuclear modification factor,  $R_{AA}$ ,

$$R_{AA} = \frac{1}{N_{binary}} \frac{d^2 N_{AA}/dp_T d\eta}{d^2 N_{pp}/dp_T d\eta} \quad (1.22)$$

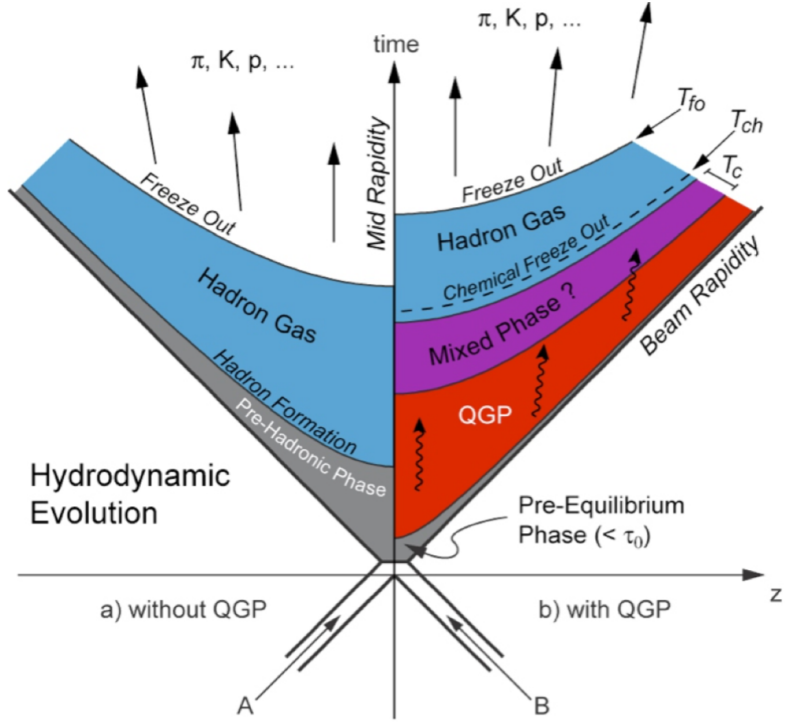


**Figure 1.12:** Comparison between a proton-proton collision with no medium and a heavy ion collision with a colored medium stage[39].

where  $N_{binary}$  is the number of binary collisions and is estimated using a Glauber model[41] of a nucleus while  $d^2N_{AA}/dp_T d\eta$  and  $d^2N_{pp}/dp_T d\eta$  are the spectra measured in nucleus-nucleus and proton-proton collision respectively.  $R_{AA}$  may be thought of as asking the question: Does a heavy-ion collision scale as a superposition of  $N_{binary}$  proton-proton collisions? If a heavy-ion collision simply looks like some  $N_{binary}$  factor of

Figure 1.13 shows the nuclear modification factor with  $R = 0.4$  jets in the ATLAS experiment at 5.02 TeV[42]. The different colored bands in the figure are broken into centrality<sup>5</sup>

---

<sup>5</sup>The purple 10 - 20% band denotes the most central events (i.e. the two colliding nuclei have a low impact parameter and collide nearly head-on), while the 70 - 80% red band denotes the least central events (i.e. the two colliding nuclei have a high impact parameter and barely graze one another). An in-depth discussion of centrality may be found here[43].

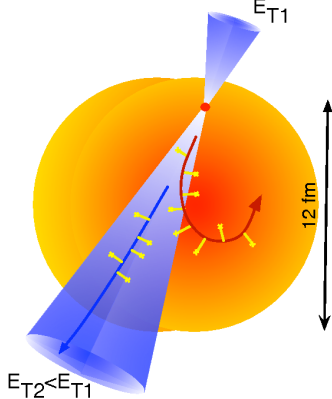


**Figure 1.13:** Jet energy loss in a QCD medium[32].

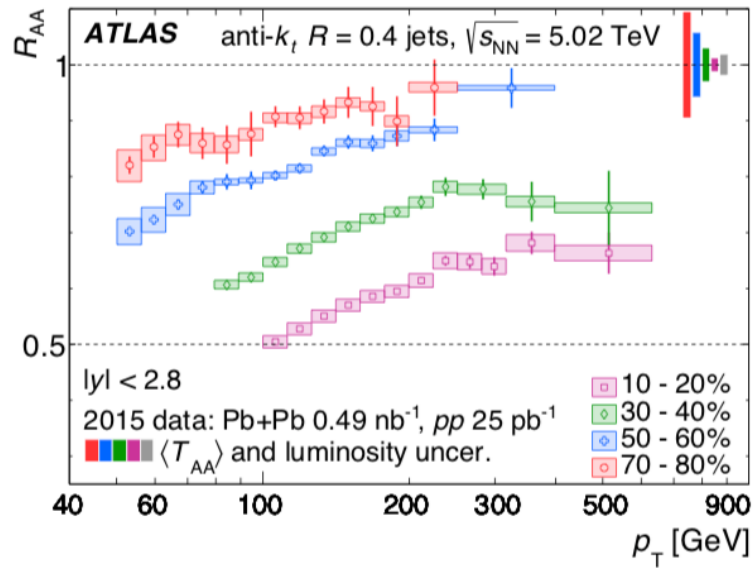


**Figure 1.14:** Jet  $R_{AA}$  at 5.02 TeV with the ATLAS experiment[42].

## 1.6 QGP in Proton-Proton Collisions?

As previously stated a QGP is believed to be absent in proton-proton collisions, thus any signature of a QGP should likewise be absent. However, one way of quantifying the presence of the QGP is via the Bjorken energy density.

$$\varepsilon = \frac{1}{\tau A} \frac{dE_T}{d\eta} \quad (1.23)$$

where  $A$  is the transverse area of the nuclei,  $\tau$  is the proper time, and  $dE_T/d\eta$  is the transverse energy per unit pseudorapidity. It can be shown that the 150 MeV critical temperature need

for the phase transition to the QGP corresponds to 1 - 3 GeV/ $fm^3$  energy density. The quantity  $dE_T/d\eta$  can be related to the mean transverse momentum  $\langle p_T \rangle$  and particle multiplicity<sup>6</sup> per unity pseudorapidity as:

$$\frac{dE_t}{d\eta} \approx \langle p_T \rangle \frac{dN}{d\eta} \quad (1.24)$$

where  $\langle p_T \rangle$  is the mean transverse momentum and  $dN/d\eta$  is the particle multiplicity per unit pseudorapidity. This suggests that in very high multiplicity proton-proton events signatures of the QGP may be present. Although suppression has never been observed in high multiplicity proton-proton collisions physicists have recently measured collective flow in such systems[44]. CMS presented collective flow results in proton-proton collisions at 13 TeV using soft-particles,  $p_T \leq 2$  GeV/ $c$ , consistent with hydrodynamical predictions[45]. These results have opened new debates and questions into the very nature of the QGP and whether jets can be used to enlighten our understanding in such systems will make up a very active and interesting segment of high energy physics research in the coming years.

---

<sup>6</sup>Multiplicity is defined as the number of particles per event

# Chapter 2

## Jet Results and Discussion

Beginning in March of 2012, the LHC began seven months of pp collisions at  $\sqrt{s} = 8$  TeV. The jet cross sections and ratios of the cross sections for jets of different radii offers a unique perspective on the pQCD effects of hadronization at this new energy frontier. Due to the expectation that no QGP is formed in a pp collision these measurements serve as a baseline for separating phenomena associated with the QGP in heavy-ion collisions. In order to measure the jet cross section the following formula is used,

$$\frac{d^2\sigma^{jet}}{d\eta dp_T} = \frac{A_{trigger}}{\epsilon_{trigger}(p_T)} \times C_{MC} \times \frac{1}{A(p_T)} \times \frac{1}{\mathcal{L}_{int}} \times \frac{dN^{jet}}{dp_T d\eta} \quad (2.1)$$

where,

- $A_{trigger}$  is the acceptance for EMCal triggered events and  $\epsilon_{trigger}(p_T)$  is the EMCal trigger efficiency. These factors correct for imperfections in the electronics of the EMCal and the overall factors are equal to one in minimum bias events.
- $C_{MC}$  is a correction factor due to detector effects and it allows for comparisons between the ALICE experiment to other experiments or theoretical calculations. Unfolding is used to determine this factor.
- $\mathcal{L}_{int}$  is the integrated luminosity during the period when the data was recorded.
- $A(p_T)$  is the geometrical detector acceptance.

- $\frac{dN^{jet}}{dp_T d\eta}$  is the inclusive jet momentum spectra.

Furthermore, it is useful to define the ratio of cross sections,

$$\mathcal{R}(p_T; R_1, R_2) = \frac{d^2\sigma(p_T; R_1)/d\eta dp_T}{d^2\sigma(p_T; R_2)/d\eta dp_T} \quad (2.2)$$

where  $\sigma(p_T; R_1)$  refers to the doubly differential cross section (Equation 2.5) of a jet with radius  $R_1$ . The ratio is carried out on a bin-by-bin basis per each  $p_T$  bin.

## 2.1 Raw Jet Spectra

This thesis reports inclusive jet results for radii between 0.1 and 0.5. Furthermore, jet results for radii  $R = 0.2$  and  $R = 0.4$  will be presented in the body of this chapter while results from the other radii will be limited to the appendix. Figure shows the raw (uncorrected)  $p_T$  spectra for inclusive jets from both MB and EMCAL triggered data. It is also evident from Figure that the EMCAL triggered data extends the  $p_T$  reach

## 2.2 Inclusive Jet Spectra and Cross Section Ratios at 2.76 TeV

Inclusive jet spectra and cross section ratios were measured in the ALICE experiment using a 2011 pp 2.76 TeV data sample[46]. Jets were reconstructed using TPC tracks and EMCAL clusters with the FastJet Anti- $K_T$  algorithm. Tracks with a minimum  $p_T \geq 150$  MeV and constrained to within 10 cm of the primary vertex were accepted into the jet finder. EMCAL clusters were

## 2.3 8 TeV Data Quality

ALICE is a state-of-the-art experiment with excellent tracking and particle identification capabilities as discussed in Chapter ???. However, just like any real world experiment, it contains a number of inefficiencies and imperfections. This means that the data collected

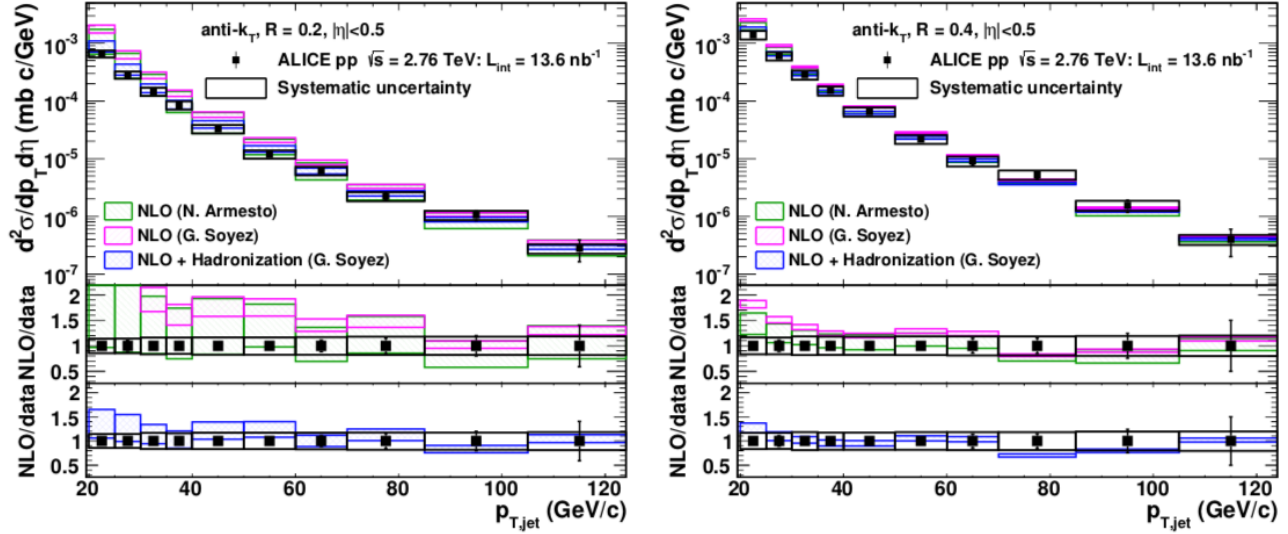


**Figure 2.1:** Inclusive differential cross section from the 2.76 TeV proton proton run with ALICE

during the 8 TeV pp collision must be examined and any inaccuracies in the data must be removed before hard physics conclusions may be reached. Data may be compromised at both the event-level, the experiment erroneously recorded something as an event, or at the constituent-level, one of the subdetectors mismeasured a feature of a particle, and these outliers must be accounted for and removed

## 2.4 Event Selection

For an event to be selected into a physics analysis it must pass a number of quality control tests. For example, the LHC must have be in a state of stable beams, cosmic rays must be excluded by only accepting tracks that originate from a vertex inside the detector, and the relevant detectors for a given analysis must be functioning as intended. Event selection and QA is implemented via a centralized class, AliEventCuts, within the AliRoot framework. This class contains a number of corrections including:

- 
- Another entry in the list

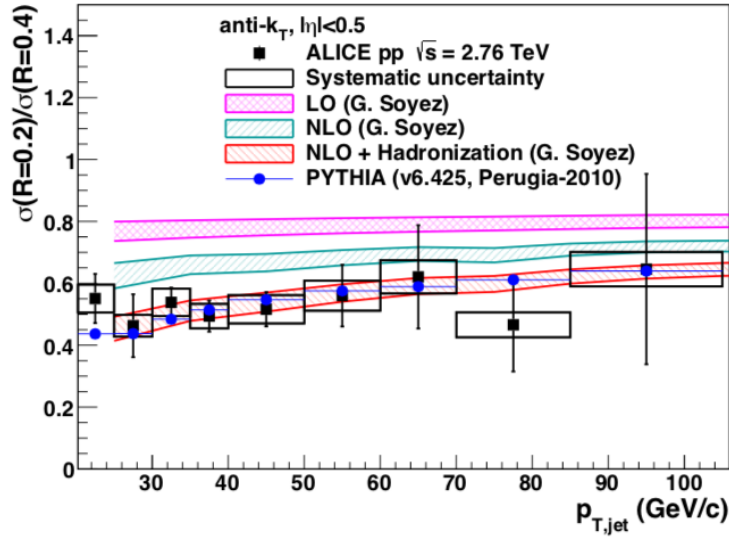


**Figure 2.2:** LHC state during the 8 TeV run.

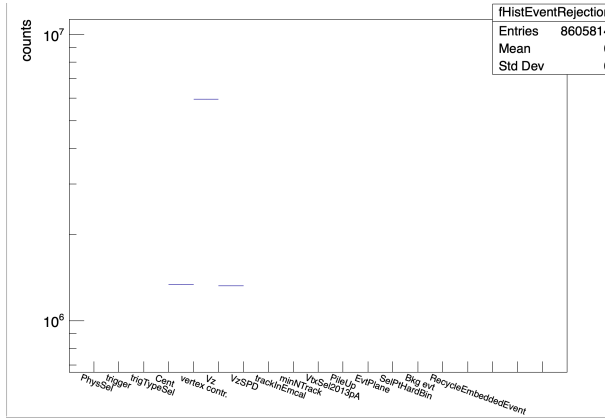


**Figure 2.3:** Minimum Bias Event Rejection

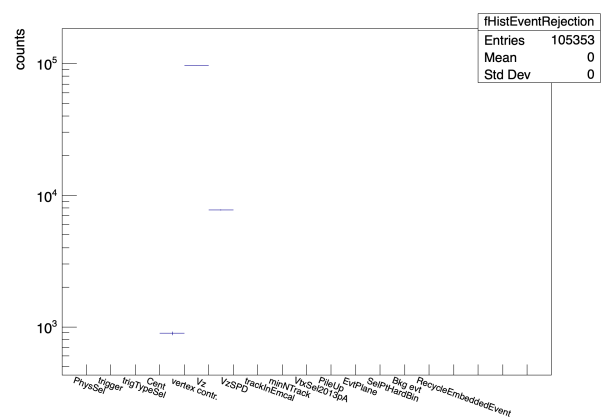


**Figure 2.4:** Emcal Triggered Event Rejection

Further more the class AliAnalysisTaskEmcalCorrection within the AliRoot framework performs a number of corrections to the tower-level within physics analysis dependent on the EMCAL. These corrections include:

- Energy calibration: Remove double counting due to the amount of energy typically deposited by a Hadron.
- Bad Channel Map: Remove both dead and hot towers from the EMCAL clusterize based on an iterative average energy per occupancy algoritham

- Time Calibration: Remove slow particles, such as neutrons, which readout to the EMCAL after the event has been recorded.
- Exotics Correction: Remove inefficiencies due to how a particle interacted with the EMCAL.

After the above cuts are performed on EMCAL towers the cells compromising the towers are clustered together using a clusterization algoritham

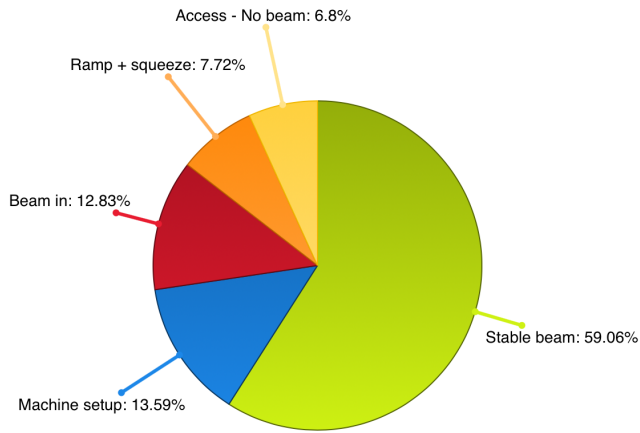


**Figure 2.5:** LHC state during the 8 TeV run.

During the 8 TeV data collection period approximately 180 million minimum bias events were recorded, as summarized in table ???. These events are separated into periods, which dictate the particular beam and detector configurations during the data taking. The 8 TeV data is broken into 7 periods with approximately 181 million minimum bias events recorded. This minimum bias sample corresponds to an integrated luminosity,  $\mathcal{L}_{int}$ , of  $8.95 pb^{-1}$  during this time period[47].

Approximately, 15% of the data sampled is unusable due to malfunctions in TPC chambers, EMCAL super modules, the electronics for the EMCAL or TPC, and

## 2.5 Raw measurements

The ALICE experiment is capable of two types of jet reconstruction, charged and full jets. Charged jets use information from the charged particle tracking detectors, such as the ITS and TPC, in conjunction with a jet finding algorithm to identify jets. Full jets implement a similar procedure but also incorporates the EMCal in order to

### 2.5.1 Raw Jet Momentum Spectra in pp Collisions

### 2.5.2 Acceptance Correction

Jet spectra, cross sections, and ratios of cross sections are reported over the full azimuth angle and pseudorapidity acceptance. However, due to jets being constrained to the EMCal, a geometric factor is used to correct for the limited acceptance of the detector. This thesis uses a maximum jet radius of 0.5 to help study the effects of wide angle radiation on jet fragmentation. Heavy-ion use smaller jet radii, typically of 0.2, to help negate the high multiplicity background. Due to these geometric corrections the centroid of a jet is constrained to,

$$|\eta_{jet}| \leq 0.7 - R, \quad 1.4 + R \leq \phi_{jet} \leq 3.14 - R. \quad (2.3)$$

$$A(p_T) = \frac{(1.4 - 2R) \times (1.745 - 2R)}{2\pi}. \quad (2.4)$$

Period	# of runs	# of Min Bias events
LHC12c	89	$\sim 24$ M
LHC12d	140	$\sim 62$ M
LHC12e	5	$\sim 2$ M
LHC12f	56	$\sim 15$ M
LHC12g	8	$\sim 0.4$ M
LHC12h	159	$\sim 75$ M
LHC12i	40	$\sim 3$ M
Total	497	$\sim 181$ M

**Table 2.1:** 2012 8 TeV data taking period.

For jets between  $R = 0.1$  through  $R = 0.5$  the following jet acceptance corrections are used.

Jet R	$A(p_T)$
0.1	0.296
0.2	0.214
0.3	0.146
0.4	0.091
0.5	0.048

**Table 2.2:** EMCal jet acceptance for radii 0.1 - 0.5.

## 2.6 Unfolding

The reconstructed jet  $p_T$  has a number of detector effects ‘folded’ into the measurement. In order to have results which can be compared to theoretical calculations or between experiments these effects must be accounted and corrected. ‘Unfolding’ is the method by which these results are corrected by and it accounts for a number of effects including; tracking and momentum inefficiencies associated with the tracking detectors, material loss in the detector, hadronic corrections in the EMCal, gaps in the acceptance of the detector and dead regions. Unfolding corrects the detector-level reconstructed jet spectra to the truth-level hadronic spectra by constructing a response matrix. In this analysis the response matrix is constructed by propagating the truth-level particle jets generated from a MC simulation through a GEANT 3 simulation of the detector during the time period that the data taking occurred. The particle-level jet centroid  $(\phi_{part}, \eta_{part})$  is matched to the detector-level jet via a constraint on the displaced distance between the two jet centroids in  $(\phi, \eta)$ . This distance was constrained to:  $\Delta R = \sqrt{(\phi_{part} - \phi_{det})^2 + (\eta_{part} - \eta_{det})^2} \leq 0.25$  for  $R = 0.3$  to  $R = 0.5$  jets and  $\Delta R \leq 0.1$  for  $R = 0.1$  and  $R = 0.2$  jets.

### 2.6.1 Corrections to particle Level

### 2.6.2 Unfolding Matrix

### 2.6.3 Unfolded Spectra

## 2.7 EMCal Triggered Data

In addition with the minimum bias data collected, the EMCal was used during the 8 TeV run in order to provided an enhanced data set that is preferential to hard processes. The Level-1 trigger[48] in the EMCal has a associated trigger,  $\epsilon$ , of

$$\epsilon = \frac{N_{events}^{Triggered}}{N_{events}^{MinBias}} \times \frac{d^2 N_{Triggered}^{jet}}{d\eta dp_T} \Bigg/ \frac{d^2 N_{MinBias}^{jet}}{d\eta dp_T} \quad (2.5)$$

## 2.8 Systematic Uncertainties

### 2.8.1 Systematic Uncertainty to Jet Yield

### 2.8.2 Systematic Uncertainty to Jet Energy Scale

#### Luminosity Uncertainty

The luminosity of a hadronic collider,  $\mathcal{L}$ , is given by the expression

$$\mathcal{L} = \frac{R}{\sigma} \quad (2.6)$$

The luminosity along with its uncertainty were determined during a a special Van der Meer scan run in April of 2012[47]. The total systematic uncertainty was obtained by measuring the visible cross section using the T0 and V0 detectors. The Uncertainty was found to be 2.36% with the T0 and 2.60% with the V0. A combined average uncertainty of 2.48% is used in this thesis.

### **2.8.3 Total Uncertainty**

## **2.9 Corrected pp jet cross section**

### **2.9.1 Comparisons to pQCD predictions**

### **2.9.2 Jet Cross Sections and Ratios**

# Chapter 3

## Conclusion and Outlook

### 3.1 8 TeV Inclusive Jet Results from CMS and ATLAS

CMS[49] and ATLAS[50] both reported the double differential cross section for inclusive jets at 8 TeV.

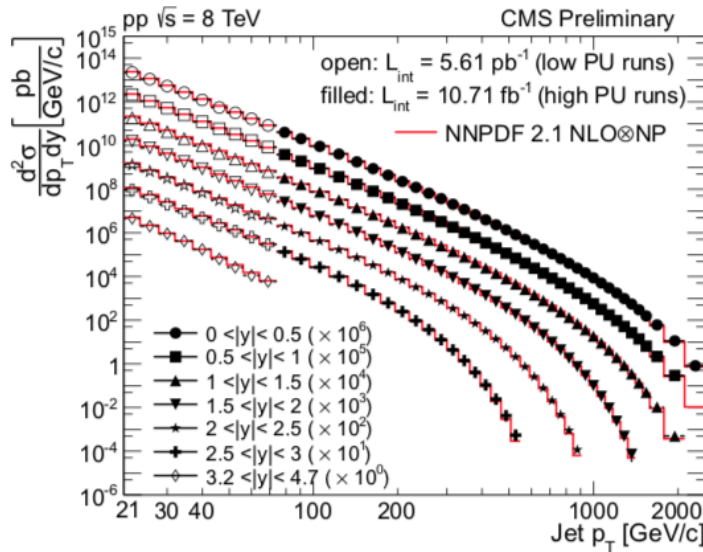


**Figure 3.1:** 8 TeV CMS inclusive jet cross sections with radii of  $R = 0.7$  and binned by jet rapidity compared to NLO calculations with non-perturbative corrections[49].

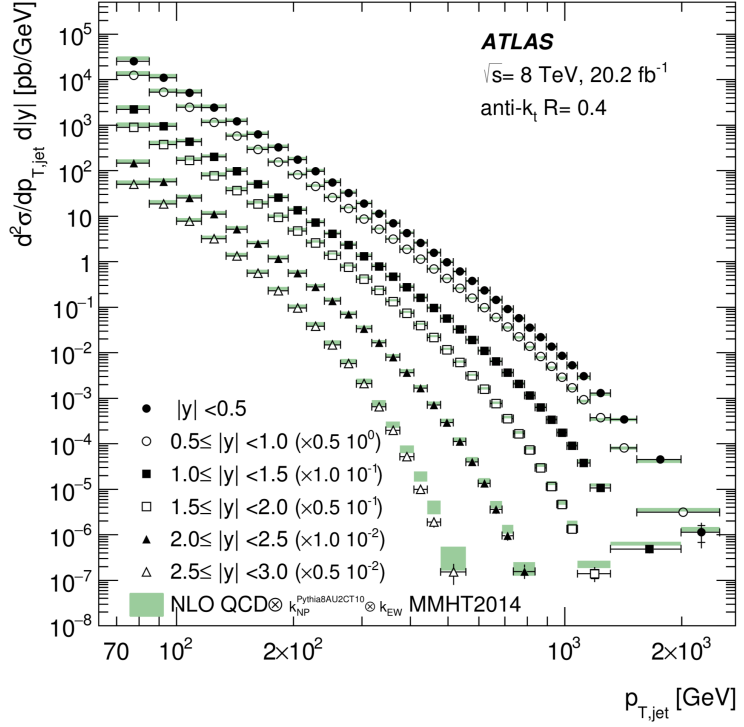


**Figure 3.2:**  $R = 0.4$  inclusive jet cross section at 8 TeV from ATLAS in binned by jet rapidity compared to NLO QCD predictions[50].

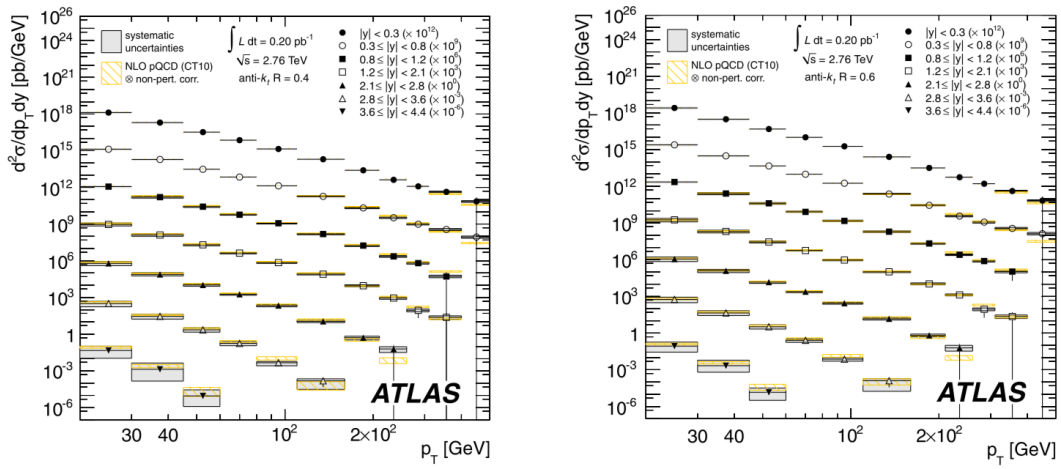


**Figure 3.3:** The 8 TeV ATLAS jet cross sections rescaled to better show comparisons with NLO and non-perturbative calculations at low  $p_T$ [50].

# Bibliography

- [1] Michael Riordan. The discovery of quarks. *Science*, 256(5061):1287–1293, 1992. [1](#)
- [2] Frank Wilczek. Asymptotic freedom: From paradox to paradigm. *Proc. Nat. Acad. Sci.*, 102:8403–8413, 2005. [Rev. Mod. Phys.77,857(2005)]. [2](#)
- [3] Vardan Khachatryan et al. Measurement of the inclusive 3-jet production differential cross section in proton–proton collisions at 7 TeV and determination of the strong coupling constant in the TeV range. *Eur. Phys. J.*, C75(5):186, 2015. [2](#)
- [4] Jets at cms and the determination of their energy scale, July 2012. [3](#)
- [5] J. D. Bjorken. Asymptotic sum rules at infinite momentum. *Phys. Rev.*, 179:1547–1553, Mar 1969. [3](#)
- [6] J. D. Bjorken. Can We Measure Parton Parton Cross-Sections? *Phys. Rev.*, D8:4098, 1973. [3](#)
- [7] Matt Dobbs and Jorgen Beck Hansen. The HepMC C++ Monte Carlo event record for High Energy Physics. *Comput. Phys. Commun.*, 134:41–46, 2001. [5](#)
- [8] Wolfgang Kurt Hermann Panofsky. Low q electrodynamics, elastic and inelastic electron (and muon ) scattering. 1968. [6](#)
- [9] J. Feltesse. Introduction to Parton Distribution Functions. *Scholarpedia*, 5(11):10160, 2010. revision #186761. [6](#)
- [10] K. Kovarik, T. Jezo, A. Kusina, F. I. Olness, I. Schienbein, T. Stavreva, and J. Y. Yu. CTEQ nuclear parton distribution functions. *PoS*, DIS2013:274, 2013. [6](#)
- [11] Richard D. Ball, Valerio Bertone, Stefano Carrazza, Christopher S. Deans, Luigi Del Debbio, Stefano Forte, Alberto Guffanti, Nathan P. Hartland, José I. Latorre, Juan Rojo, and Maria Ubiali. Parton distributions for the LHC Run II. *JHEP*, 04(arXiv:1410.8849. EDINBURGH 2014-15. IFUM-1034-FT. CERN-PH-TH-2013-253. OUTP-14-11P. CAVENDISH-HEP-14-11):040. 138 p, Oct 2014. Comments: 138 pages, 64 figures. Several typos in text and references corrected, one reference added. [6](#)

- [12] Harald Fritzsch. QCD: 20 years later. In *QCD 20 Years Later: Proceedings, Workshop, Aachen, Germany, June 9-13, 1992*, pages 827–852, 1992. [7](#)
- [13] John C. Collins, Davison E. Soper, and George F. Sterman. Factorization of Hard Processes in QCD. *Adv. Ser. Direct. High Energy Phys.*, 5:1–91, 1989. [7](#)
- [14] Nora Brambilla, Xavier Garcia i Tormo, Joan Soto, and Antonio Vairo. The Logarithmic contribution to the QCD static energy at  $N^{**}4$  LO. *Phys. Lett.*, B647:185–193, 2007. [7](#)
- [15] Martin Erdmann. Investigation of quark - anti-quark interaction properties using leading particle measurements in e+ e- annihilation. *Phys. Lett.*, B510:29–35, 2001. [7](#)
- [16] B. R. Webber. Hadronization. In *Proceedings: Summer School on Hadronic Aspects of Collider Physics, Zuoz, Switzerland, Aug 23-31, 1994*, pages 49–77, 1994. [8](#)
- [17] Bo Andersson, Sandipan Mohanty, and Fredrik Soderberg. Recent developments in the Lund model. In *36th Annual Winter School on Nuclear and Particle Physics (PINP 2002) and 8th St. Petersburg School on Theoretical Physics St. Petersburg, Russia, February 25-March 3, 2002*, 2002. [9](#)
- [18] B. R. Webber. A QCD Model for Jet Fragmentation Including Soft Gluon Interference. *Nucl. Phys.*, B238:492–528, 1984. [9](#)
- [19] L. L. Jenkovszky, V. K. Magas, J. T. Londergan, and A. P. Szczepaniak. Explicit Model Realizing Parton-Hadron Duality. *Int. J. Mod. Phys.*, A27:1250157, 2012. [10](#)
- [20] Jan Rak and Michael J. Tannenbaum. *QCD in hard scattering*, pages 214–243. Cambridge Monographs on Particle Physics, Nuclear Physics and Cosmology. Cambridge University Press, 2013. [10](#)
- [21] Ryan Atkin. Review of jet reconstruction algorithms. *J. Phys. Conf. Ser.*, 645(1):012008, 2015. [11](#), [14](#)
- [22] J E Huth, N Wainer, K Meier, N J Hadley, F Aversa, Mario Greco, P Chiappetta, J P Guillet, S Ellis, Zoltán Kunszt, and Davison Eugene Soper. Toward a standardization of jet definitions. (FERMILAB-CONF-90-249-E):7 p, Dec 1990. [11](#)

- [23] Gerald C. Blazey et al. Run II jet physics. In *QCD and weak boson physics in Run II. Proceedings, Batavia, USA, March 4-6, June 3-4, November 4-6, 1999*, pages 47–77, 2000. [11](#)
- [24] Matteo Cacciari, Gavin P. Salam, and Gregory Soyez. FastJet User Manual. *Eur. Phys. J.*, C72:1896, 2012. [15](#)
- [25] Megan Connors, Christine Nattrass, Rosi Reed, and Sevil Salur. Jet measurements in heavy ion physics. *Rev. Mod. Phys.*, 90:025005, 2018. [16](#)
- [26] R Brun, F Bruyant, M Maire, A C McPherson, and P Zanarini. *GEANT 3: user’s guide Geant 3.10, Geant 3.11; rev. version*. CERN, Geneva, 1987. [16](#)
- [27] Torbjorn Sjostrand, Stephen Mrenna, and Peter Z. Skands. A Brief Introduction to PYTHIA 8.1. *Comput. Phys. Commun.*, 178:852–867, 2008. [16](#)
- [28] Peter Zeiler Skands. Tuning Monte Carlo Generators: The Perugia Tunes. *Phys. Rev.*, D82:074018, 2010. [17](#)
- [29] A. Capella, U. Sukhatme, C.-I. Tan, and J. Tran Thanh Van. Dual parton model. *Physics Reports*, 236(4):225 – 329, 1994. [17](#)
- [30] Cheuk-Yin Wong. *Introduction to high-energy heavy-ion collisions*. World Scientific, Singapore, 1994. Erratum. [17](#)
- [31] Fritz W. Bopp, R. Engel, and J. Ranft. Rapidity gaps and the PHOJET Monte Carlo. In *High energy physics. Proceedings, LAFEX International School, Session C, Workshop on Diffractive Physics, LISHEP’98, Rio de Janeiro, Brazil, February 16-20, 1998*, pages 729–741, 1998. [17](#)
- [32] Bedangadas Mohanty. Exploring the QCD phase diagram through high energy nuclear collisions: An overview. *PoS*, CPOD2013:001, 2013. [18](#), [21](#)
- [33] T. Csorgo. New form of matter at CERN SPS: Quark matter but not quark gluon plasma. *Nucl. Phys. Proc. Suppl.*, 92:62–74, 2001. [,62(2000)]. [18](#)

- [34] I. Arsene et al. Quark gluon plasma and color glass condensate at RHIC? The Perspective from the BRAHMS experiment. *Nucl. Phys.*, A757:1–27, 2005. [18](#)
- [35] K. Adcox et al. Formation of dense partonic matter in relativistic nucleus–nucleus collisions at rhic: Experimental evaluation by the {PHENIX} collaboration. *Nuclear Physics A*, 757(1–2):184 – 283, 2005. First Three Years of Operation of {RHIC}. [18](#)
- [36] B.B. Back et al. The {PHOBOS} perspective on discoveries at {RHIC}. *Nuclear Physics A*, 757(1–2):28 – 101, 2005. First Three Years of Operation of {RHIC}. [18](#)
- [37] J. Adams et al. Experimental and theoretical challenges in the search for the quark–gluon plasma: The {STAR} collaboration’s critical assessment of the evidence from {RHIC} collisions. *Nuclear Physics A*, 757(1–2):102 – 183, 2005. First Three Years of Operation of {RHIC}. [18](#)
- [38] Barbara V. Jacak and Berndt Müller. The exploration of hot nuclear matter. *Science*, 337(6092):310–314, 2012. [18](#)
- [39] J. D. Bjorken. Highly relativistic nucleus-nucleus collisions: The central rapidity region. *Phys. Rev. D*, 27:140–151, Jan 1983. [20](#)
- [40] Shanshan Cao, Tan Luo, Guang-You Qin, and Xin-Nian Wang. Heavy and light flavor jet quenching at rhic and lhc energies. *Physics Letters B*, 777:255 – 259, 2018. [19](#)
- [41] Michael L. Miller, Klaus Reygers, Stephen J. Sanders, and Peter Steinberg. Glauber modeling in high energy nuclear collisions. *Ann. Rev. Nucl. Part. Sci.*, 57:205–243, 2007. [20](#)
- [42] Morad Aaboud et al. Measurement of the nuclear modification factor for inclusive jets in Pb+Pb collisions at  $\sqrt{s_{\text{NN}}} = 5.02$  TeV with the ATLAS detector. *Phys. Lett.*, B790:108–128, 2019. [20](#), [21](#)
- [43] Klochkov and I Selyuzhenkov and. Centrality determination in heavy-ion collisions with the CBM experiment. *Journal of Physics: Conference Series*, 798:012059, jan 2017. [20](#)

- [44] James L. Nagle and William A. Zajc. Small System Collectivity in Relativistic Hadronic and Nuclear Collisions. *Ann. Rev. Nucl. Part. Sci.*, 68:211–235, 2018. [22](#)
- [45] Wenbin Zhao, You Zhou, Hao jie Xu, Weitian Deng, and Huichao Song. Hydrodynamic collectivity in proton–proton collisions at 13 tev. *Physics Letters B*, 780:495 – 500, 2018. [22](#)
- [46] Rongrong Ma. Measurements of the inclusive jet cross section and jet fragmentation in pp collisions with the alice experiment at the lhc. *Nuclear Physics A*, 910-911:319 – 322, 2013. Hard Probes 2012. [24](#)
- [47] ALICE luminosity determination for pp collisions at  $\sqrt{s} = 8$  TeV. Mar 2017. [28](#), [31](#)
- [48] O. Bourrion, R. Guernane, B. Boyer, J. L. Bouly, and G. Marcotte. Level-1 jet trigger hardware for the ALICE electromagnetic calorimeter at LHC. *JINST*, 5:C12048, 2010. [30](#)
- [49] CMS Collaboration. Measurement of the double-differential inclusive jet cross section at  $\text{sqrt}(s) = 8$  TeV with the CMS detector. 2013. [32](#)
- [50] Morad Aaboud et al. Measurement of the inclusive jet cross-sections in proton-proton collisions at  $\sqrt{s} = 8$  TeV with the ATLAS detector. *JHEP*, 09:020, 2017. [32](#), [33](#)

# Appendices

# Vita